Supporting Information

# Wood Waste-derived Dual-Mode Materials Paving the Way for Year-Round Energy Saving in Buildings

*Jiayi Zhang,*[1] *Kairen Yin,* [1] *Zirui Zhuang,* [1] *Jinghan Zhou,* [1] *Yixi Tang,* [1] *Jingyong Xu,* [1] *Yipeng Chen,* [1,*] *Yingying Li,*[1,*] *Qingfeng Sun*[1,*]

[1] College of Chemistry and Materials Engineering, Zhejiang A&F University, Hangzhou, Zhejiang Province, 311300, P.R. China

*Corresponding author: Yipeng Chen (zafucyp@163.com), Yingying Li (yyli@zafu.edu.cn), Qingfeng Sun (qfsun@zafu.edu.cn)

## 1. Materials and Methods

**1.1 Materials.** Henan Province Jiaozuo National Forestry Farm supplied the raw materials, wood fiber. Sinopharm Chemical Reagent Co., Ltd supplied NaOH, $Na_2SO_3$, $CaCl_2$, $CH_3COOH$, methyl alcohol, epoxy chloropropane, and anhydrous ethanol; Aladdin supplied sodium alginate (Shanghai, China), TEMPO, $Na_2ClO$, and $Ca(NO_3)_2$.

**1.2 Fabrication of cellulose and sodium lignosulfonate.** An appropriate quantity of wood fiber was added to the mixed solution of 2.5 M NaOH and 0.4 M $Na_2SO_3$, and the hydrothermal reaction was conducted for eight hours at 80°C, and collect the solution after the reaction. The wood fiber treated in the first step was added to a solution of 0.12 M NaClO mixed with 0.08 wt.% of analytically pure $CH_3COOH$, and the solution was changed every hour for eight hours. The resulting wood fiber was placed in a 2.5 M $H_2O_2$ solution heated at 100 °C for 8 h and then repeatedly washed with deionized water to obtain cellulose.

The liquid collected during the preparation of cellulose was adjusted to a PH 3 with $H_2SO_4$ at a concentration of 10 %, held for 10-20 min, and then dried by centrifugation at 4000 rpm in a CHRIST centrifuge to obtain alkaline lignin. Weigh 10.95 wt% of alkaline lignin with 2.74 M NaOH and heat and stir to 85°C until dissolved. Subsequently, a solution of $H_2O_2$ with a mass fraction of 30% in a volume ratio of 17% was added. After the reaction at constant temperature for 1 h, 0.168 M $Na_2SO_3$ and 7% by volume methyl alcohol were added. The temperature was increased to 90°C, and the reaction was constant for 3 h, followed by rotary evaporation of the liquid at 85 °C. The resulting product was dried at 60 °C to obtain sodium

lignosulfonate.

**1.3 Fabrication of dual-mode thermal managing structural material.** After mixing 100 mL of 15 mg/mL lignosulfonate solution with 0.5wt% sodium alginate solution, 10 mL epichlorohydrin was added to crosslink the lignosulfonate saline gel precursor. Tempo oxidized cellulose hydrogel and lignosulfonate saline gel were prepared by dipping the precursor and Tempo oxidized cellulose into 0.1M $CaCl_2$ solution, respectively. Finally, multi-layer TEMPO-oxidized cellulose hydrogel and lignosulfonate saline gel were hot-pressed at 40 MPa and 90 °C to produce wood-based dual-mode passive radiation thermostatic structural material.

**1.4 Characterization.** SEM images were taken with a Carl Zeiss Supra 40 (5 kV). The FTIR spectrometer (model 6700, Thermo Fisher Scientific) measured infrared properties at a 12 angle of incidence using a diffuse gold integrating sphere. The reflectivity (ρ) and transmittance (τ) of the samples were determined using FTIR, and the emissivity (ε) was calculated based on $\varepsilon = 1 - \rho - \tau$. At room temperature, the ultraviolet absorption spectra of the materials were determined using a double beam UV-Vis spectrophotometer (TU-1901, PERSEE). The acoustic absorption and insulation testing were conducted using the impedance tube (Test-Material-CIT30/100) developed by BOACH Acoustics. Performance evaluation was carried out according to the standards GB/T 18696.2-2002 and GB/Z 27764, utilizing an impedance tube with an internal diameter of Φ30/100mm. Porosity testing was performed following the ISO 5017 standard.

**1.5 Mechanical measurement.** The three-point bending test of the sample was

carried out using MTS-1. The samples were approximately 10mm in diameter and 2 mm thick, with a 40 mm measurement span and a displacement velocity of 1 mm $min^{-1}$. The samples were subjected to an impact toughness test using the SMT-3009C pendulum impact testing machine. The sample was approximately 50 mm in length, about 10 mm in width, and around 2 mm in thickness. All mechanical tests are performed on each specimen five times, with the loading direction perpendicular to each layer.

**1.6 Thermal measurement.** All test samples were cut into squares with sides of 100mm, placed in EPS hot boxes, and covered with transparent PE film. The internal temperature of our hot box and the outside environment temperature were monitored using thermocouples coupled to a multi-loop control system (TPC7062TX, KunLunTongTai). The DRP-II thermal conductivity tester measured dual-mode, ceramic, and concrete thermal conductivity. All samples were Φ 130. To assess the temperature variations induced by photothermal processes in the heating surface, we utilized an 808 nm semiconductor laser emitter (PerkinElmer Inc., USA) as the light source. Simultaneously, an infrared camera (FLIR Systems, Inc., USA) served as the temperature detection device to monitor temperature changes. Solar light was monitored using a xenon lamp (Beijing China Education Au-light Co., Ltd). The power density ($W \cdot cm^{-2}$) denotes the light intensity per unit area ($cm^{-2}$) irradiated on the sample, adjusted by varying the distance between the light source and the sample. The optical power meter (NP2000, Beijing China Education Au-light Co., Ltd) facilitated the measurement of power density. Temperature data were recorded at 10-second

intervals, with a defined temperature modulation cycle lasting 7 minutes (comprising a 4-minute heating phase and a 3-minute cooling phase).

**1.7 Thermal-electric conversion test.** The heating layer, cooling layer and thermoelectric module constituted a thermoelectric generator (TEG) employed to evaluate the photo-thermal-electric conversion. Illumination from the xenon lamp induced a temperature differential across the heating layer, leading to the activation of the Seebeck effect and the generation of electrical energy. The produced power was utilized to operate an electric fan. By adjusting the power density of the xenon lamp, voltage fluctuations were measured using a voltmeter, and the corresponding fan speed was recorded.

**1.8 Building energy simulation.** Energy consumption and energy savings were predicted using EnergyPlus 8. We referenced the building models defined by the U.S. Department of Energy (pre-1980) in EnergyPlus and customized our model accordingly. The simulation model incorporated design specifications for HVAC systems, lighting, and windows, with a total area of 1567 $m^2$ and windows covering 7.5% of the total wall area. Internal air temperature was set at a constant 22°C, and external weather data were obtained from Typical Meteorological Year (TMY) and California Climate Zones 2 (CTZ2) datasets provided by the National Renewable Energy Laboratory and California Energy Commission, respectively. Moreover, 16 cities represent 16 climate zones in the United States: Albuquerque, Austin, Boulder, Chicago, Duluth, Durham, Fairbanks, Helena, Honolulu, Las Vegas, Los Angeles, Minneapolis, New York City, Phoenix, San Francisco, and Seattle. Using the U.S.

Department of Energy definition of a post-1980 mid-rise apartment, calculations were performed. The model building has two floors, and for the temperature boundary condition, the indoor air temperature set-point is 18°C in winter and 26°C in summer. The baseline energy usage for heating and cooling may be determined by applying the model to the whole United States.

**1.9 Finite element model simulation.** A two−dimensional (2D) nonlinear finite element model is developed using the commercial software ABAQUS 2022. In the simulation, a 2D Voronoi structure (250 × 60 μm$^2$) is adopted, as shown in Figure S13. The cells with isotropic bulk modulus $E_p$=7 GPa, Poisson ratio $v_p$ = 0.3 and the failure strength $\sigma_p^m$ = 60 MPa bear elastic deformation before brittle failure.

**2. The dual-mode heat managing structural materials' thickness Settings.**

In order to understand the basic mechanism of the dual-mode heat managing structural materials, the radiative heat flux ($q_{rad}$) of our materials to the environment is considered (Eq. (1)).

$$q_{rad} = \frac{\sigma\left(T_{sam}^{\ 4} - T_{amb}^{\ 4}\right)}{\frac{1}{\varepsilon_{sam}} + \frac{1}{\varepsilon_{amb}} - 1} \approx \sigma\varepsilon_{sam}\left(T_{sam}^{\ 4} - T_{abm}^{\ 4}\right) \quad (1)$$

$q_{rad}$: Heat flow radiated by materials to an atmospheric window.

$\sigma$: Stefan-Boltzmann constant.

$\varepsilon_{amb} \approx 1$: Ambience emissivity.

$\varepsilon_{sam}$: Ambience emissivity.

$T_{sam}$: Sample surface temperature.

$T_{amb}$: The temperature of the ambiance.

As the chemical composition of the cooling surface and the heating surface is similar, there is almost a difference in emission rate. In cooling mode, the cooling surface faces the environment, and the thickness from the cooling surface to the interior is small (the heating surface is thin). This small thickness ensures effective heat transfer between the interior and the cooling surface. Thus increasing the efficiency of heat loss (higher $T_{sam}$). When the material is flipped, the side of the heating surface faces outward, and the distance from the lignin surface to the interior increases, resulting in a decrease in thermal conductivity (lower $T_{sam}$), so the material is in heating mode.

**3. Radiative cooling performance**

To quantify the radiative cooling performance of radiative coolers, we calculate the cooling power at different temperature T. According to energy balance theory, the net radiative cooling power can be calculated with the following equation:

$$P_{cool}(T) = P_{rad}(T) - P_{sun} - P_{atm}(T_{amb}) - P_{non-rad}, \quad (2)$$

where $T_{\mathrm{amb}}$ is the ambient temperature. In Eq. (2), the radiative power emitted by per area of coating ($P_{\mathrm{rad}}(T)$), the absorbed power of coating due to incident atmospheric thermal radiation ($P_{\mathrm{atm}}(T_{\mathrm{amb}})$), the absorbed power of coating due to incident solar radiation ($P_{\mathrm{sun}}$), and the non-radiative absorbed power ($P_{\mathrm{non\text{-}rad}}$) due to convection and conduction can be calculated by:

$$P_{rad}(T) = \int_0^{\infty} \int_0^{2\pi} \int_0^{\frac{\pi}{2}} \varepsilon(\lambda, \theta) I_{bb}(T, \lambda) \sin\theta \cos\theta \, d\varphi \, d\lambda, \quad (3)$$

$$P_{atm}(T_{amb}) = \int_0^{\infty}\int_0^{2\pi}\int_0^{\frac{\pi}{2}} \varepsilon_{atm}(\lambda,\theta) I_{bb}(T_{amb},\lambda)\sin\theta\cos\theta d\varphi d\lambda \quad , \tag{4}$$

$$P_{sun} = \int_0^{\infty} \varepsilon(\lambda,\theta_{sun}) \cdot I_{AM1.5}(\lambda) d\lambda \quad , \tag{5}$$

$$P_{non-rad} = h_c(T_{amb} - T), \tag{6}$$

where $I_{bb}(T, \lambda)$ is the spectral blackbody intensity, $\varepsilon(\lambda, \theta)$ is the spectral directional emissivity, $\varepsilon_{atm}(\lambda, \theta) = 1\text{-}t(\lambda, 0)^{1/cos\theta}$. $I_{AM1.5}(\lambda)$ is the solar radiance with direct normal irradiance, for the calculation of non-radiative heat transfer, we initially assume that $h_c$ = 6.9 W/(m$^2$ K). To quantify the radiative cooling performance of coatings shown above, two parameters can be used to quantify the performance. One is the lowest temperature the coating can achieve when the net radiative cooling power is zero ($P_{net}$ = 0). The other is the net radiative cooling power when the temperature of coating is the same as ambient temperature ($T = T_{amb}$).

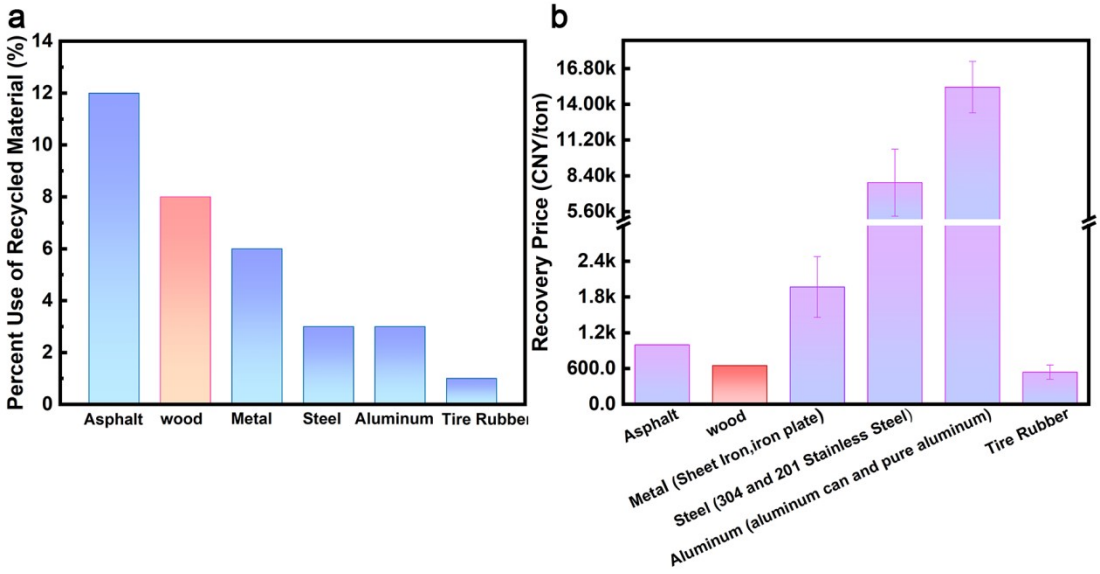


**Fig. S1.** Utilization Rates and Market Recycling Prices of Various Common Recycled Structural Materials. (a) Utilization rates of recycled asphalt, wood, metals, steel, aluminum, and tire rubber. (b) Market recycling prices of discarded asphalt, wood, metals, steel, aluminum, and tire rubber as of March 31, 2024 (China example). It is worth noting that the price data above are sourced from unofficial Chinese waste resource recycling trading platforms, provided by Shanghai Neng Information Technology Co., LTD, and are indicative and effective.

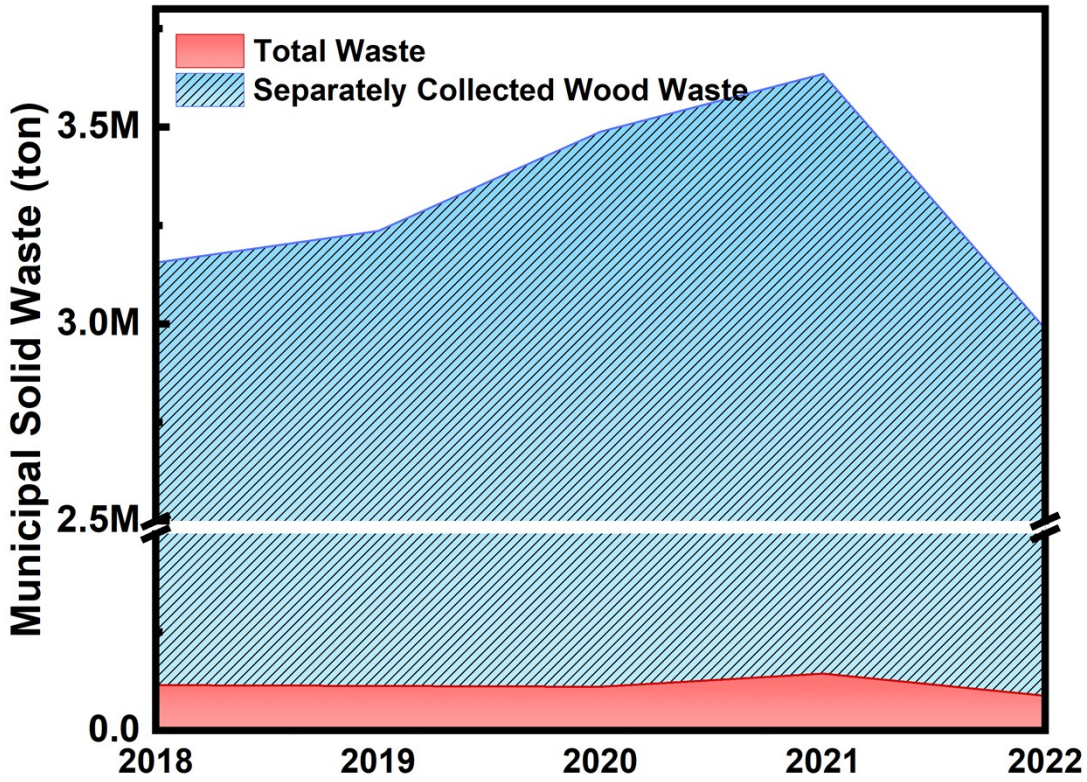


**Fig. S2.** Urban Solid Waste Statistics in Finland (2018-2022).


**Fig. S3.** The wood processing residue is put into a colloidal mill to grind into a fibrous pulp. The wood fiber is treated with sodium hydroxide and sodium sulfite, and the waste liquid after filtration is treated to get sodium lignosulfonate. The treated wood fibers are bleached and pulped to obtain cellulose.

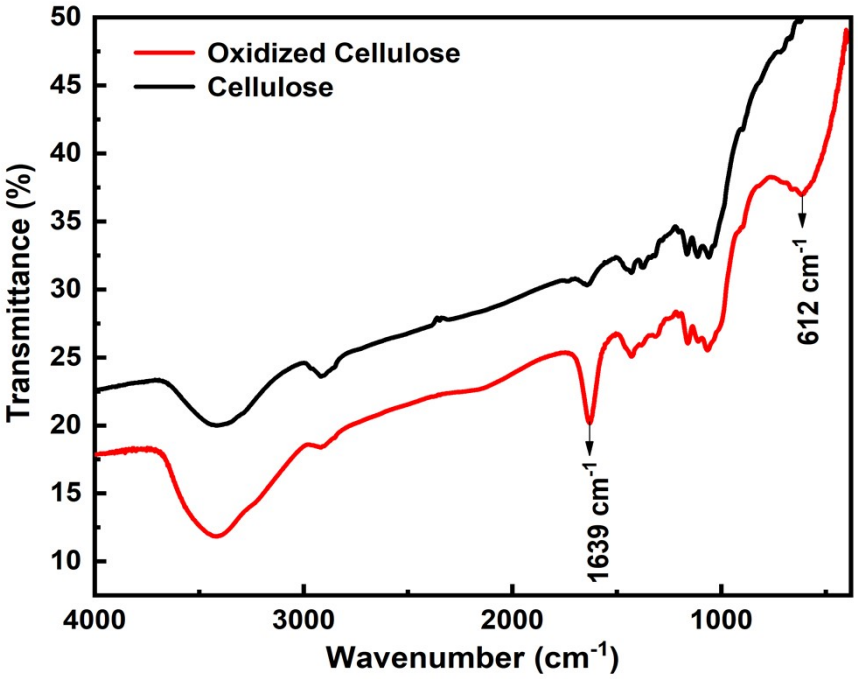


**Fig. S4.** FTIR image comparison of pure cellulose and tempo-oxidized cellulose. Compared with the FTIR image of pure cellulose, the absorption peak of 1639 $cm^{-1}$ of oxidized cellulose became sharpened and enhanced, indicating the increase of the carboxyl group in the sample, while the carboxyl bent vibration band also appeared at 612 $cm^{-1}$.

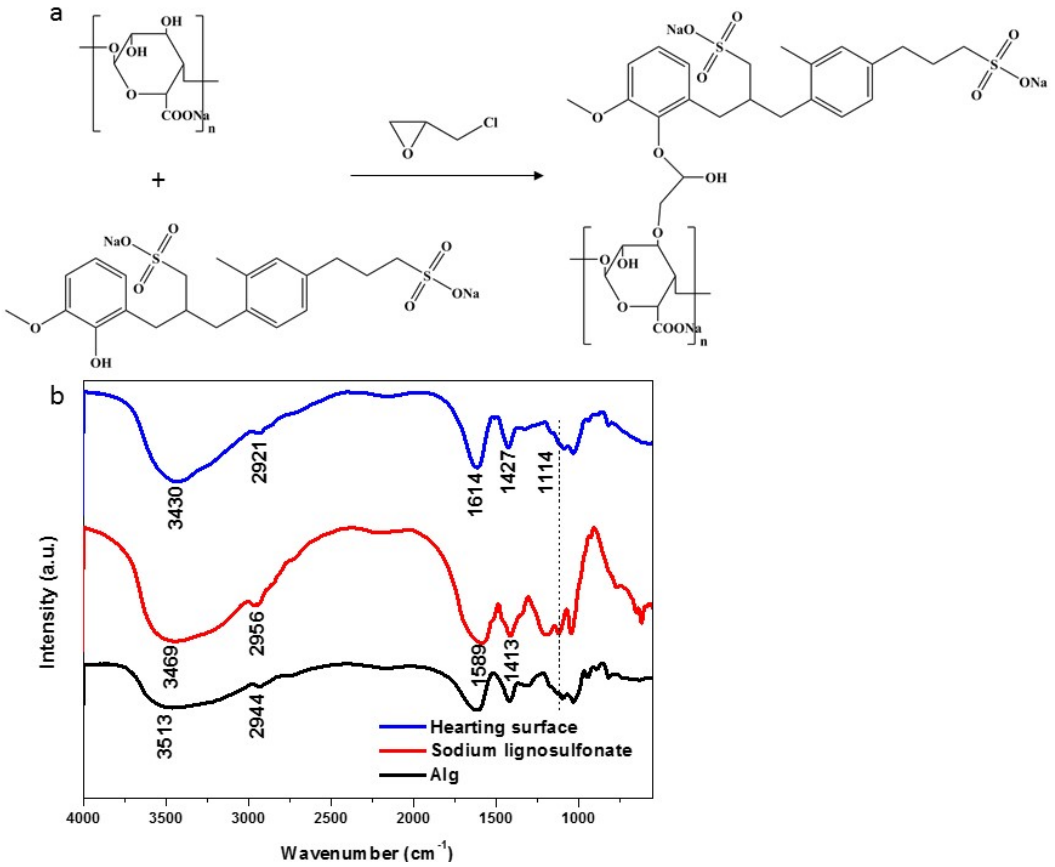


**Fig. S5.** (a) Synthesis of epoxy chloropropane cross-linked lignin sodium sulfonate/alginate, (b) Infrared spectra of alginate, lignin sodium sulfonate, and (heating surface) sodium sulfonate/alginate. The broad peak around 3430 $cm^{-1}$ is attributed to the O-H stretching vibration absorption peak, and its shift to the lower wavenumber indicates that a considerable portion of -OH has undergone a reaction. The peak at 2921 $cm^{-1}$ corresponds to the stretching vibration of C-H. The peaks at 1614 $cm^{-1}$ and 1427 $cm^{-1}$ represent the skeletal stretching vibrations of the benzene ring. The intensity of the absorption peak around 1095 $cm^{-1}$, related to the -C-O-C- bond, significantly increases, further indicating the generation of a substantial amount of ether bonds.

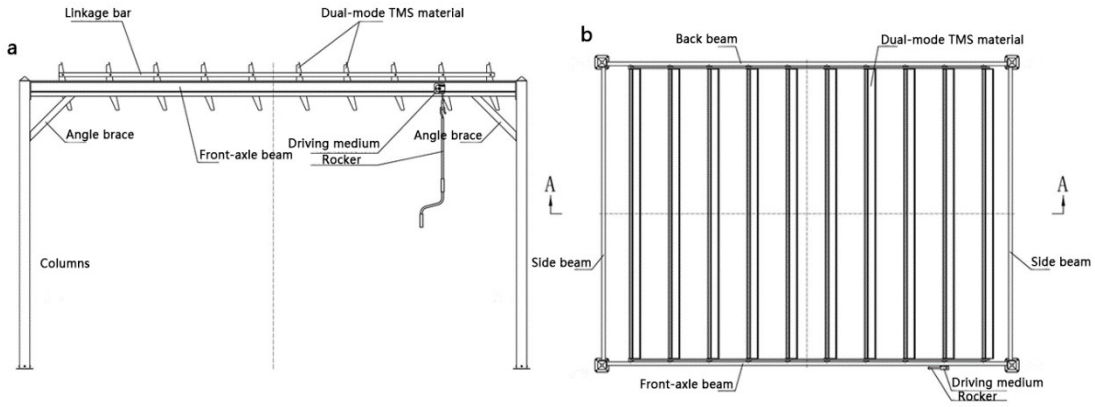


**Fig. S6.** The (a) front view and (b) top view of the reversible tile structure. It includes brackets and tiles, with the brackets supported by four pillars under a quadrangular frame formed by front and rear beams and two measurements. Tiles are uniformly laid in the quadrangular frame. The tiles are connected between the front and rear beams through pivot shafts, where tiles on the same pivot shaft form the same row, and tiles in the same straight line along the front beam direction constitute the same column. One side of the tile is equipped with a connection hole for the tile linkage rod, and the tile linkage rod is fixed in the same column of tiles through the connection hole. There is a pipe cavity at the midpoint of the tile, with small holes on the pipe cavity. The pivot shaft is a hollow shaft, and the small holes communicate with the hollow pivot shaft. The front beam and pillars are tubular structures, and the through-holes of the front beam and pillars are connected. The ends of the hollow pivot shaft are inserted into the shaft holes of the front and rear beams to install the tiles on the brackets. The tiles rotate along the pivot shaft through the worm and worm gear transmission. The worm and worm gear transmission are controlled by a crank rocker mechanism.

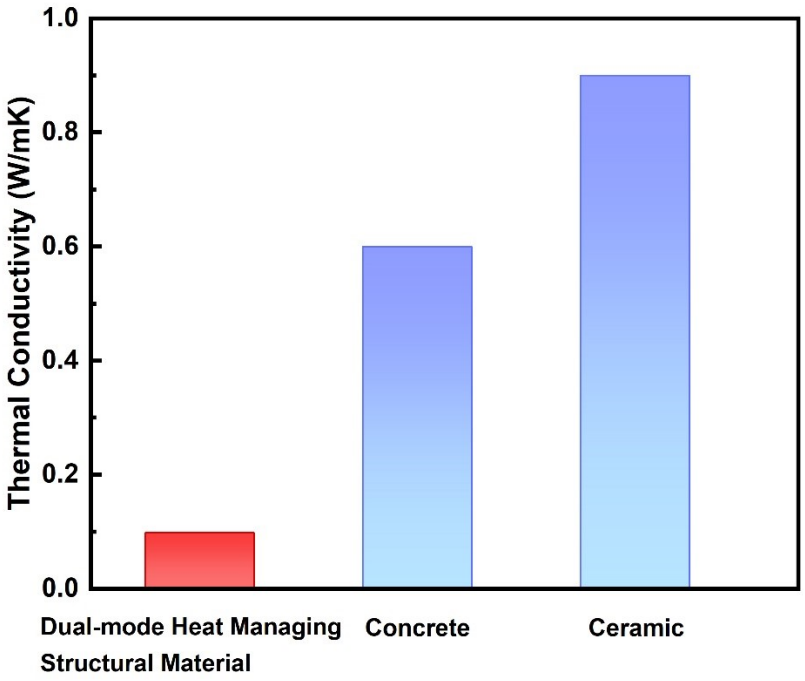


**Fig. S7.** The thermal conductivity of dual-mode heating managing structural material, concrete and ceramic[1, 2].

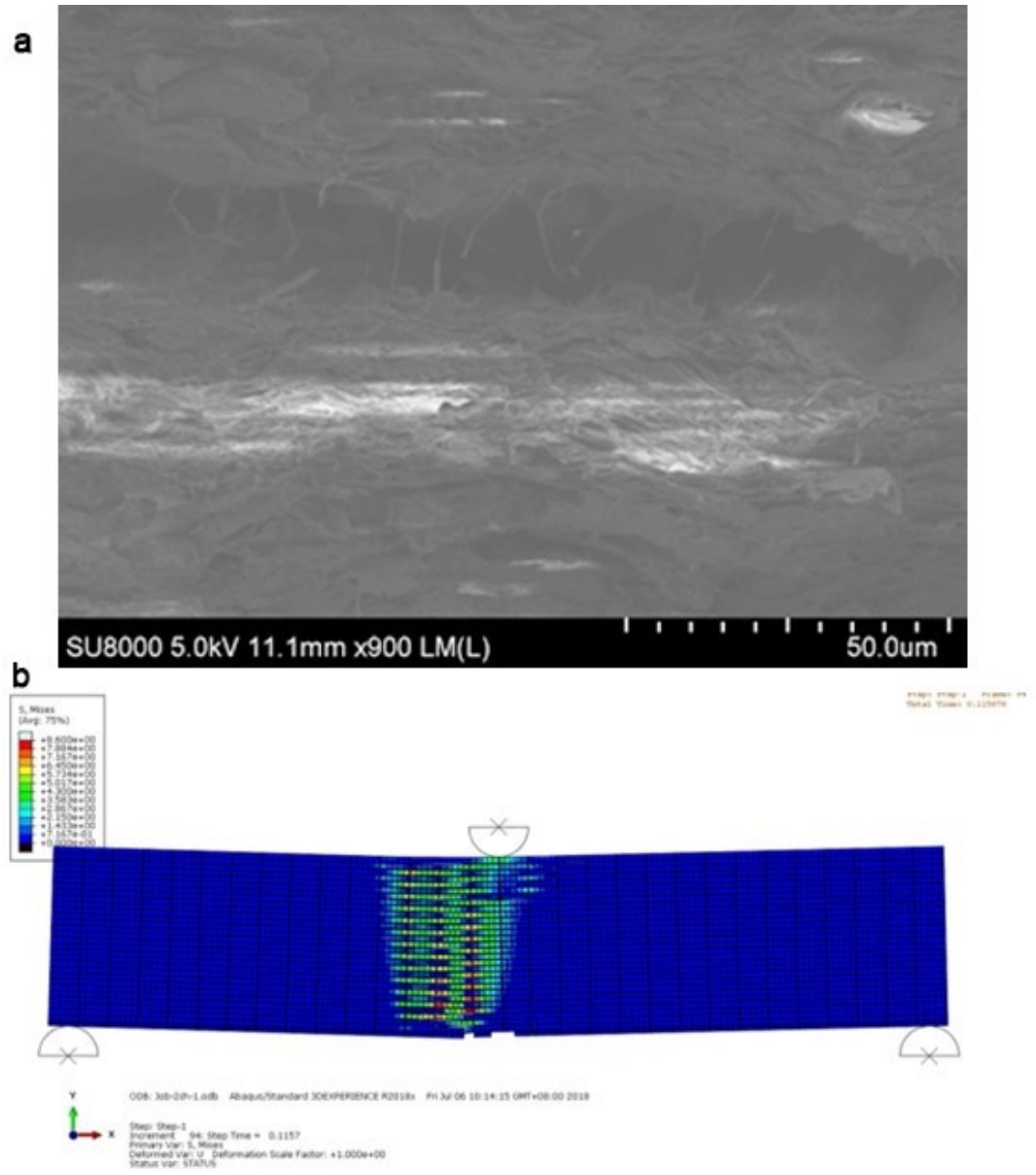


**Fig. S8.** (a) SEM image of fiber pull-out. (b) Finite element method (FEM) simulation of the behavior of the dual-mode TMS material.

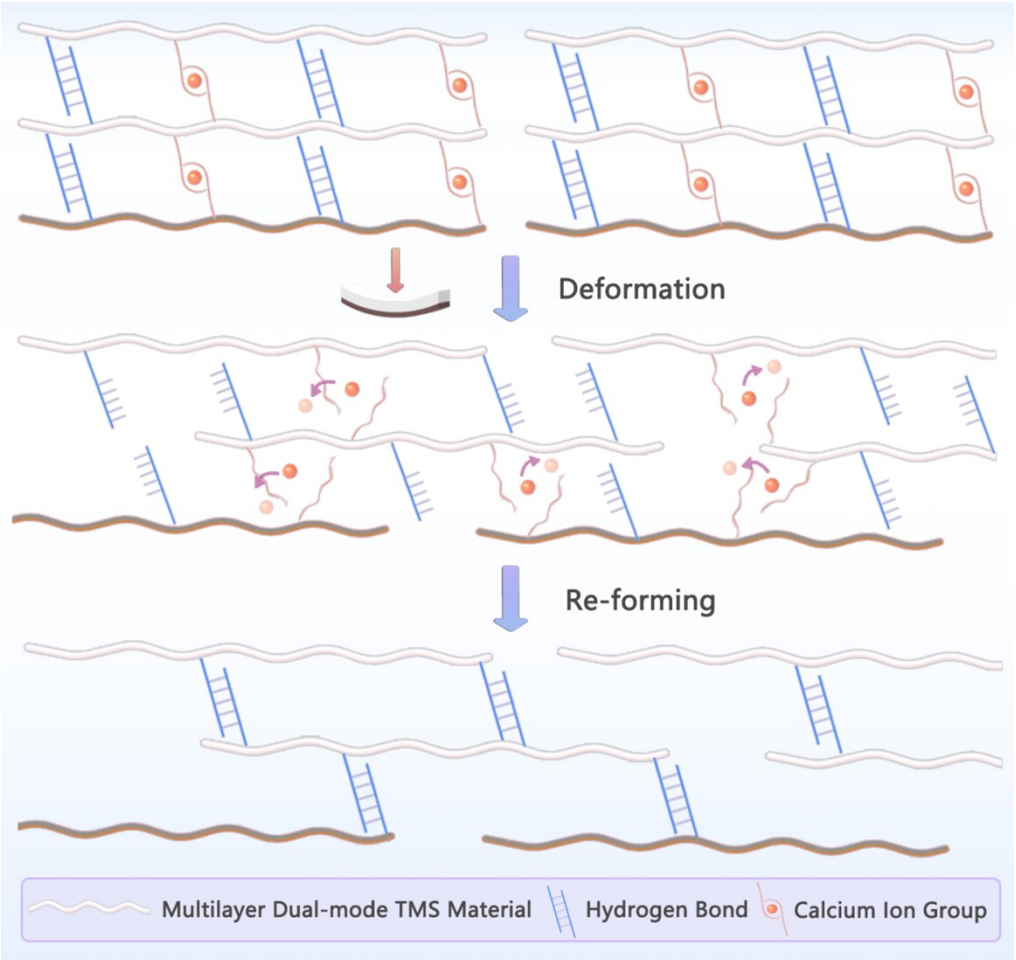


**Fig. S9.** Toughening mechanism of dual-mode TMS material under external force

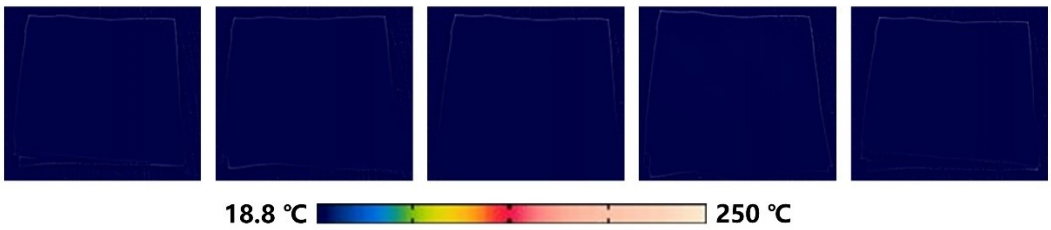


**Fig. S10**. Infrared thermal imaging images of pure sodium alginate irradiated under different light power densities.


**Fig. S11.** On a bright sunny day in Hangzhou, China (30°14′45.08″ N, 120°10′41.70″ E, 15.90 m height), the thermal box was utilized to quantify the radiative heating temperature.

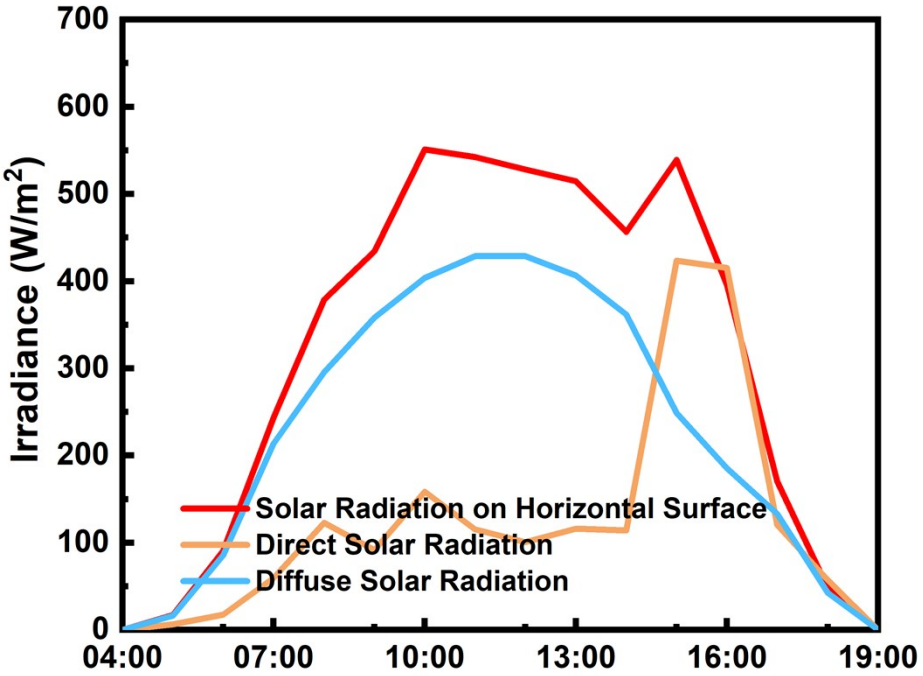


**Fig. S12.** Solar irradiance on the day of the outdoor test.[3]

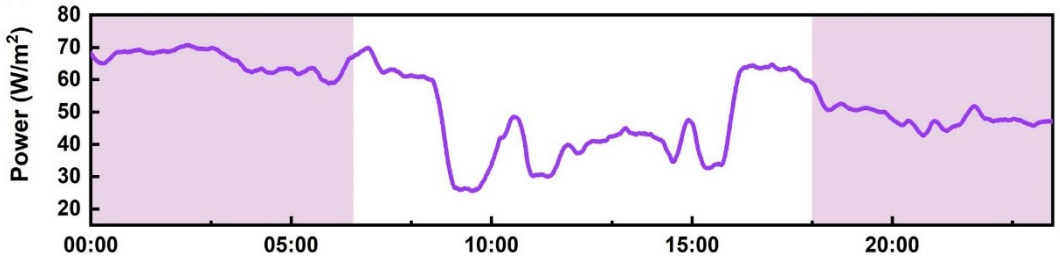


**Fig. S13.** The measurement of cooling power in twenty-four-hour of dual-mode heat managing structural material.

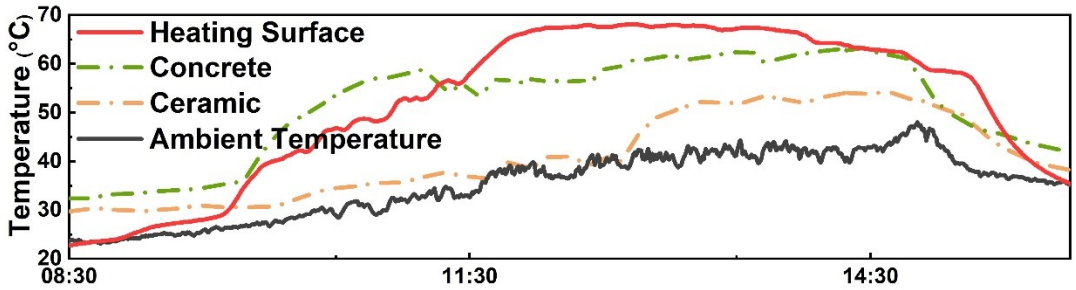


**Fig. S14**. A monitoring of the surface temperature of a dual-mode TMS material, concrete, ceramic, and the ambient temperature.

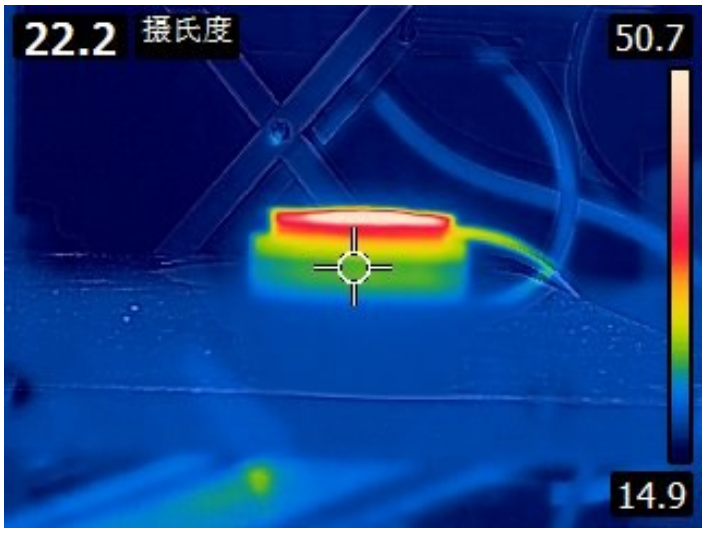


**Fig. S15.** Infrared images of the TEG under 0.1 W $cm^{-2}$ illumination.

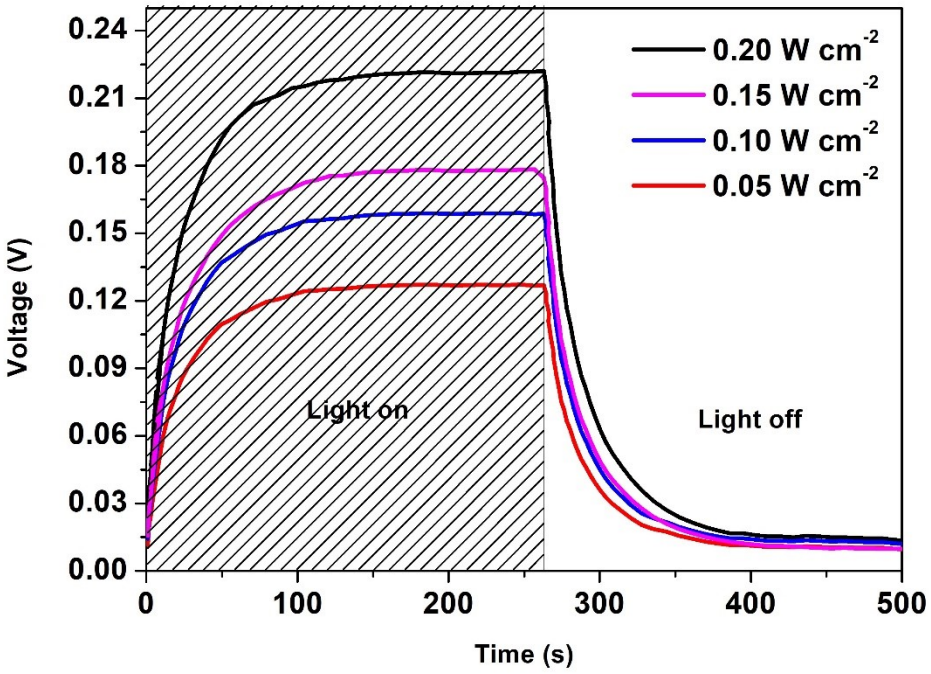


**Fig. S16.** Voltage generated by the solar TEG device under the illumination of a xenon lamp with different light power densities.

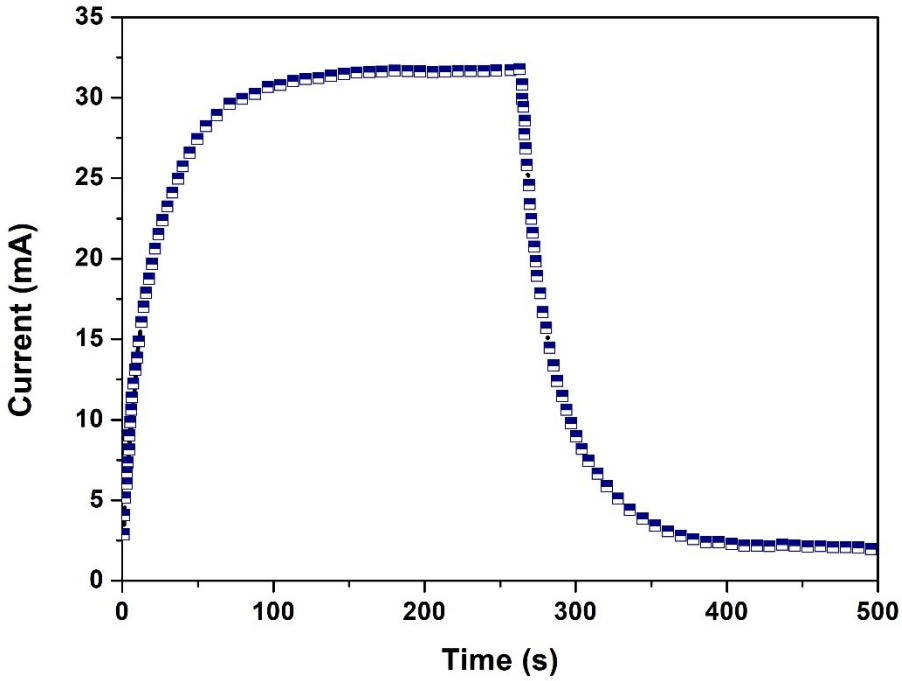


**Fig. S17.** Output current generated by the solar TEG device under the illumination of a xenon lamp with different light power densities.

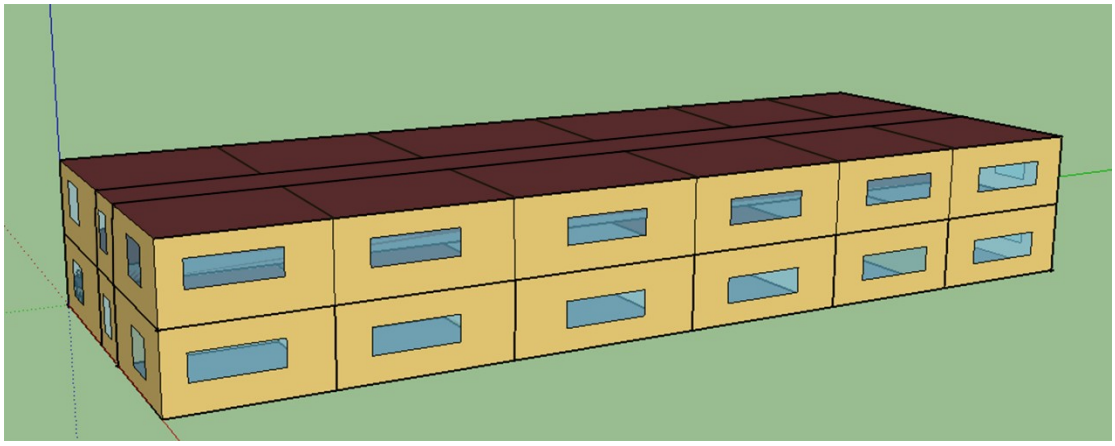

**Fig. S18.** Modeling of energy savings resulting from the installation of cooling wood panels on the roofs and exteriors of midrise residential complexes. Schematic of a midrise building.

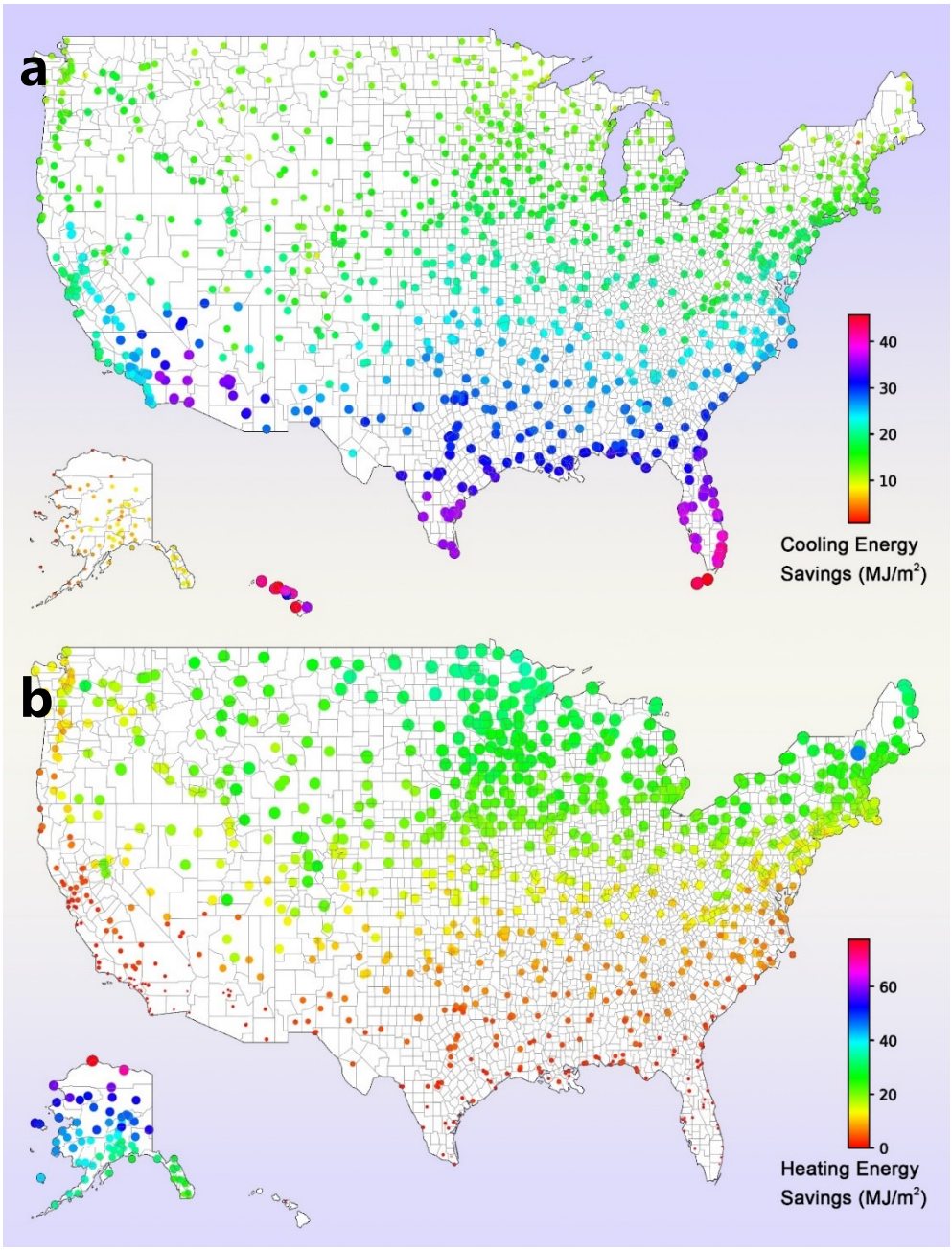


**Fig. S19.** (a) Cooling energy savings and (b) heating energy savings maps across the United States with dual-mode heat managing structural material installation on roofing for a typical midrise apartment building.

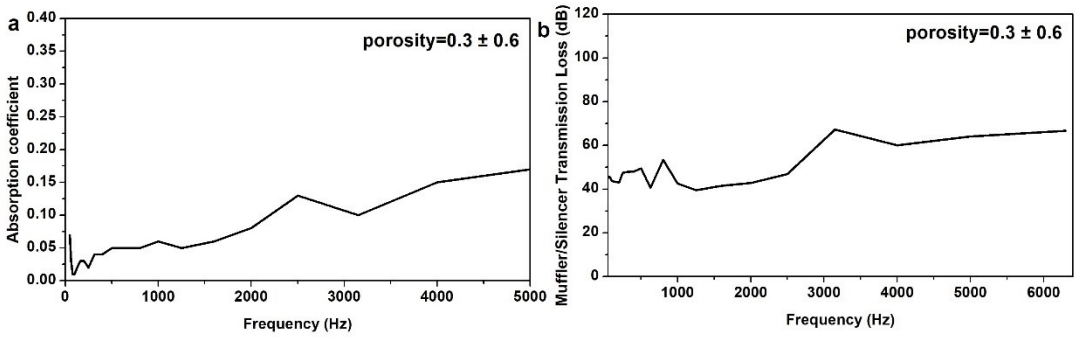


**Fig. S20.** Sound absorption coefficient test results (a) and sound insulation test results (b) of the dual-mode TMS material.

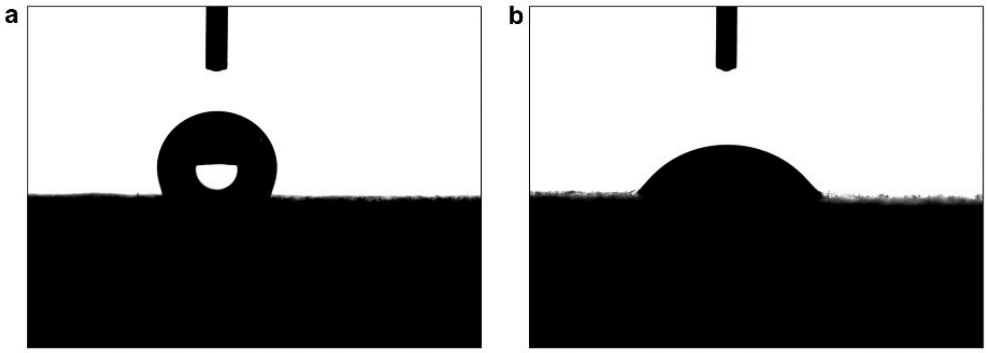


**Fig. S21.** Contact angle of heating surface (a) and cooling surface (b).

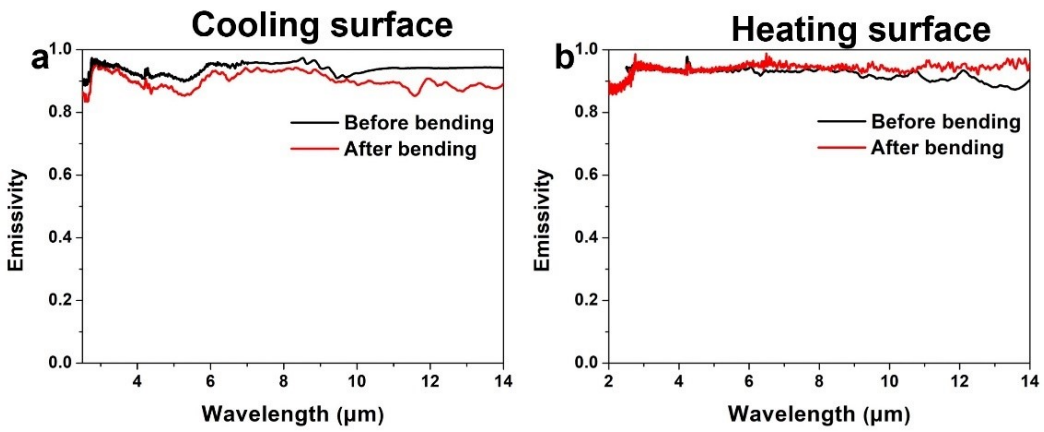


**Fig.. S22.** Change in the emissivity of cooling surface (a) and heating surface (b) after bending test.

Table S1. Thermal management properties of different materials

| Materials | Performance | Reference |
|---|---|---|
| PVDF/CA hierarchical porous coating | Annual energy saved 199,260 kWh | [4] |
| PVDF/PTFE porous polymer coating | Sub-ambient radiative cooling of 3.2 °C Above-ambient solar heating of 21.4 °C | [5] |
| PVDF porous structure | Sub-ambient temperature drop of 3.7 °C at noon | [6] |
| Porous PTFE layers with a cermet-based absorber | Annual cooling and heating savings of 77 % and 27 %, respectively | [7] |
| Porous $SiO_2$ nanoparticle coating | Temperature increase of 10 °C in cold weather Temperature reduction of 5 °C in hot weather | [8] |
| Poly(N-isopro-polyacrylamide-co-N, N-dimethyl | Temperature drop of 7.3 °C in summer Temperature increase of 3 °C in winter | [9] |

| | | |
|---|---|---|
| acrylamide) hydrogels | | |
| Layered Cellulose/lignin double-sided structural material | Sub-ambient radiative cooling of 6°C and solar heating of 27.5°C, reduce cooling energy consumption by an average of 18% and heating energy consumption by 42% | Our work |

**References**


1. B. P. Jelle, *Energy and buildings*, 2011, **43**, 2549-2563.
2. O. Sengul, S. Azizi, F. Karaosmanoglu and M. A. Tasdemir, *Energy and Buildings*, 2011, **43**, 671-676.
3. XIHE-ENERGY.COM, Technology of Digital Energy, https://www.xihe-energy.com/, (accessed 26 January, 2023).
4. J. Fei, D. Han, J. Ge, X. Wang, S. W. Koh, S. Gao, Z. Sun, M. P. Wan, B. F. Ng and L. Cai, *Adv. Funct. Mater.*, 2022, **32**, 2203582.
5. J. Mandal, M. Jia, A. Overvig, Y. Fu, E. Che, N. Yu and Y. Yang, *Joule*, 2019, **3**, 3088-3099.
6. S. Shi, P. Lv, C. Valenzuela, B. Li, Y. Liu, L. Wang and W. Feng, *Small*, 2023, **19**, 2301957.
7. X. Wang and S. Narayan, *Renewable Energy*, 2022, **197**, 574-582.

8. C. Zhang, J. Yang, Y. Li, J. Song, J. Guo, Y. Fang, X. Yang, Q. Yang, D. Wang and X. Deng, *Adv. Funct. Mater.*, 2022, **32**, 2208144.

9. G. Chen, K. Wang, J. Yang, J. Huang, Z. Chen, J. Zheng, J. Wang, H. Yang, S. Li and Y. Miao, *Adv. Mater.*, 2023, **35**, 2211716.